

Cerebrovascular segmentation of TOF-MRA based on seed point detection and multiple-feature fusion

Ruoxiu Xiao^{a,b}, Hui Ding^a, Fangwen Zhai^a, Wenjing Zhou^c, Guangzhi Wang^{a,*}

^a Department of Biomedical Engineering, School of Medicine, Tsinghua University, Room C249, Beijing, 100084, China

^b School of Computer and Communication Engineering, University of Science and Technology Beijing, Beijing, 100083, China

^c Tsinghua University Yuquan Hospital, No. 5, Shijingshan Road, Shijingshan District, Beijing, 100049, China

ARTICLE INFO

Article history:

Received 16 March 2018

Received in revised form 27 June 2018

Accepted 5 July 2018

Keywords:

Time-of-flight

Cerebrovascular segmentation

Maximum intensity projection

Seed point detection

Fuzzy inference

ABSTRACT

The accurate extraction of cerebrovascular structures from time-of-flight (TOF) data is important for diagnosis of cerebrovascular diseases and planning and navigation of neurosurgery. In this study, we proposed a cerebrovascular segmentation method based on automatic seed point detection and vascular multiple-feature fusion. First, the brain mask in the T1-MR image is detected to enable the extraction of the TOF brain structure by simultaneously acquiring the TOF image and its corresponding T1-MRI. Second, local maximum points are detected on three maximum-intensity projections of TOF-MRA data and then be traced back in three-dimensional space to detect seed points for the initialization of vascular segmentation. Third, the TOF-MRA image and its corresponding vesselness image are fused to enhance vascular features on the basis of fuzzy inference for the extraction of whole cerebrovascular structures, particularly miniscule cerebral vessels. Finally, detected seed points and multiple-feature fused enhanced images are provided to the procedure of region growing, and cerebrovascular structures are segmented. Experimental results show that compared with traditional methods, the proposed method has higher accuracy for vascular segmentation and can avoid over- and under-segmentations. The proposed cerebrovascular segmentation method is not only effective but also accurate. Therefore, it has potential clinical applications.

© 2018 Elsevier Ltd. All rights reserved.

1. Introduction

Cerebrovascular disease, which is mainly caused by vascular stenosis or aneurysm as a result of vascular malformations, is a major threat to human health. Three-dimensional time-of-flight magnetic resonance angiography (TOF-MRA) is a popular clinical cerebrovascular imaging modality given its non-invasiveness, rapidity, and high resolution. The accurate segmentation of the three-dimensional structure of blood vessels from TOF images is important for the diagnosis and quantitative analysis of cerebrovascular disease. In addition, accurate cerebrovascular segmentation is an important prerequisite for neurosurgical planning and navigation (Du et al., 2013).

Over the past two decades, numerous methods have been proposed for the segmentation of three-dimensional cerebrovascular structures from TOF-MRA (Kirbas and Quek, 2004; Lesage et al., 2009). The statistical model-based method is a typical

method for cerebrovascular segmentation and based on the principle of Bayesian statistical classification. This method constructs two grayscale distribution functions to fit the background and blood vessels in an image. The threshold for blood vessel segmentation is obtained by optimizing grayscale distribution functions. Hassouna et al. (2006) proposed a vascular segmentation method based on a statistical model. In this method, the intensity of the background and blood vessels is fitted using a Rayleigh distribution function and two normal distribution functions. Expectation maximization algorithm is utilized to optimize initial model parameters, which would converge to an optimal solution. Wen et al. (2014) introduced normal and Rayleigh functions to simulate the image background and used a normal function to fit blood vessels. Then they utilized a particle-swarm optimization algorithm to optimize the parameters of the model. Blood vessels are mainly located in an area of high intensity in a TOF-MRA dataset. Therefore, large vessels of high intensity could be easily differentiated when using a statistical model-based approach to segment blood vessels. However, some small vessels are not easily identified using statistical models because of their low intensity.

* Correspondence author.

E-mail address: wgz-dea@mail.tsinghua.edu.cn (G. Wang).

Vascular tracking is also a commonly used vascular segmentation method and operates on the principle of vascular grayscale distribution. Unlike the statistical model-based method, which uses the entire gray distribution of blood vessels in an image, vascular tracking uses the characteristics of a blood vessel's cross section, which has a Gaussian-like intensity distribution (Friman et al., 2010; Yang et al., 2009). Therefore, in this method, the grayscale distribution of a vascular cross-section is firstly fitted by tracking starting from some defined initial seed points, and vascular centerlines, diameters, and bifurcations are extracted to reconstruct the spatial structure of blood vessels (Lesage et al., 2009). For example, Aylward et al. (Aylward et al. (1996); Aylward and Bullitt, 2002) proposed a vascular segmentation method based on multi-scale ridges and the features of vascular sectional grayscale distribution. The method extracts whole vascular structures through ridge tracking on the basis of the gradient and Hessian matrix-defined vascular ridge. The tracking-based vascular segmentation method can effectively detect small vessel branches and ensure blood vessel integrity. However, extracting the section of vascular disease, where the grayscale distribution is different from Gaussian distribution, is difficult. Tracking would be prematurely terminated, resulting in an incomplete segmentation result.

Region growing is another commonly used vascular segmentation method (Masutani et al., 1998). In region growing, segmentation is based on initially defined seed points and expands iteratively to obtain the vascular area by analyzing the relationship between adjacent voxels and the segmented region until converging to the final segmentation result. Since blood vessels are connected in human's body, vascular structures can be iteratively extracted by region growing algorithm, if one or a small amount of seed points are placed on each vascular branch (Yang et al., 2014; Cong et al., 2015). Therefore, compared with previous two methods, it is more simple and effective. However, grayscale distribution within the blood vessel region is not very consistent in practice; thus, a large number of seed points have to be set to guarantee completely segmented vascular structures. In addition, manual seed point setting is not only time consuming but also cannot be replicated, and different seed points provided by different operators might result in different vascular segmentation results. Therefore, if a large number of seed points could be automatically detected and precisely located within the blood vessel, the efficiency of segmentation might be greatly improved.

Currently, only a few papers have reported the detection of seed points in three-dimensional space. The majority of related studies have focused on the detection of seed points in a two-dimensional angiographic image. For example, Fritzsche et al. (2003) proposed a seed-point detection method by extracting local maximum points on a retinal image. The image is sampled and compared with four adjacent pixels to filter out seed points. We previously (Xiao et al., 2015) proposed a seed-point detection method based on ridge-point extraction from coronary angiograms. A ridge-point detection discriminant is constructed by the gradient and Hessian matrix of pixels to extract the amount of seed points located on vascular centerlines.

If seed points are local maximum points in a three-dimensional space, then they would be also the local maximum points in a two-dimensional projection plane. In accordance with this principle, an automatic seed-point detection method based on maximum intensity projection (MIP) is proposed. First, a TOF-MRA image is projected onto a two-dimensional plane, and local maximum intensity points are extracted in the projection plane. Then, these points are traced back to the original three-dimensional space to obtain their three-dimensional positions. Compared with the method for the direct detection of seed points in a three-dimensional space, the proposed method extracts three-dimensional seed points from a two-dimensional MIP image.

In this paper, the brain region in TOF-MRA will be extracted to remove the interference of the skull during cerebrovascular segmentation. Then, seed points in the TOF-MRA image are detected using the proposed algorithm. An enhanced vesselness image can be calculated according to the Hessian matrix of the TOF-MRA image in multi-scale space because the intensity of small vascular branches is weak and difficult to detect in the original TOF image. A fuzzy interference-based vascular multiple-feature fusion method is proposed to combine the features of the TOF-MRA image and its corresponding vesselness image. Finally, all detected seed points are utilized for region growing to segment vascular structures on the enhanced vascular multiple-feature fusion image.

2. Method

The main steps of the proposed method for vascular segmentation can be divided as follows: First, the brain mask in the T1-MR image is detected to enable the extraction of the TOF brain structure by simultaneously acquiring the TOF image and its corresponding T1-MRI. Second, seed points are automatically detected in the extracted TOF brain structure. Third, the vascular multiple-feature fusion image is constructed. Finally, three-dimensional vascular structures are segmented by region growing based on the detected seed points and vascular multiple-feature fusion image.

2.1. Extraction of TOF brain structure

Non-brain regions of the skull, cerebrospinal fluid, and air are included in TOF imaging. The skull should be stripped to remove the redundant area of the TOF dataset, i.e., the detection of the brain mask in the TOF dataset, for the extraction of cerebrovascular structures. Numerous algorithms and tools, such as BEaST (Eskildsen et al., 2012), SPM (Ashburner, 2007), Freesurfer (Fischl, 2012), and FSL (Smith et al., 2004), are currently available for the accurate detection of brain mask in MR images. FSL can be used to effectively detect the brain mask in T1-MRI. In this study, we use the FSL to detect the brain mask in T1-MRI and then obtain a 0-1 volume data structure. The logic "and" operation between the output 0-1 volume data and TOF dataset is implemented to ensure that the entirety of the newly generated TOF volume dataset is within the region of the brain. Moreover, the output brain mask is processed using a mathematical morphological dilation operation to ensure that all the vessels in the cerebral cortex are completely covered by the mask.

In Fig. 1, (A) shows a slice of the obtained TOF dataset, (B) shows the result of adding the brain mask onto the original TOF slice, and (C) shows the obtained TOF brain image operated on the brain mask and TOF dataset. After preprocessing, vessels in non-brain region can be removed, and only cerebral vessel in the brain region will be detected.

2.2. Seed point detection

Seed point positing is crucial for initializing the extraction of vascular structures. This study proposes an automatic seed-point detection method. In this method, the TOF brain volume is projected onto images in the X, Y, and Z directions, and local maximum points are extracted as seed point candidates.

In Fig. 2, in the MIP of volume data $V(x, y, z)$ in the Z-axis direction, a two-dimensional projected image can be obtained on the XY plane, where the projection can be expressed as follows:

$$I_z(x, y) = \max_{z \in Z} \{V(x, y, z)\} \quad (1)$$

Let MIP in the Z-axis direction be denoted as ZMIP. In image $I_z(x, y)$, which is obtained by ZMIP, the intensity of the maximum

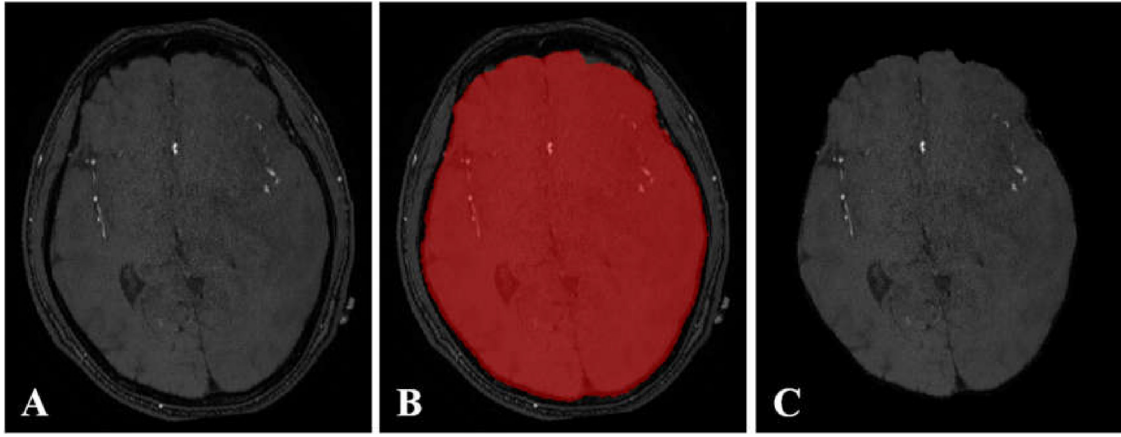


Fig. 1. (A) Slice of TOF dataset. (B) Result of adding brain mask to the original slice of TOF dataset. (C) Extracted TOF brain image.

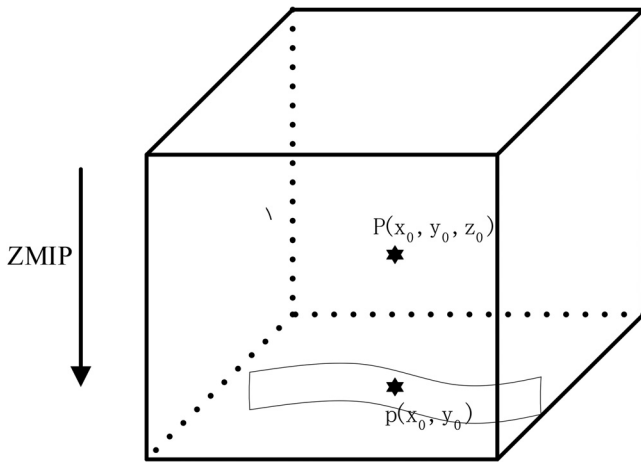


Fig. 2. MIP of three-dimensional volume in the Z-axis direction.

point $P(x_0, y_0, z_0)$ in the Z-axis direction and its spatial coordinate position are recorded. Thus, to save the Z-axis coordinate of projection point $p(x_0, y_0)$ that corresponds to $P(x_0, y_0, z_0)$, the Z-axis coordinate value of all maximum points of ZMIP are recorded in a ZBuffer image and can be expressed as follows:

$$ZBuffer(x, y) = \arg \max_{z \in Z} \{V(x, y, z)\} \quad (2)$$

In the projection of ZMIP $I_z(x, y)$, all local extreme maximum points are detected to construct the candidate seed point set $Seeds_z$:

$$Seeds_z = \left\{ (x, y, z) \mid \begin{array}{l} I_z(x, y) \geq I_z(x + \Delta x, y + \Delta x), z = ZBuffer(x, y) \\ \Delta x = -1, 0, 1 \\ \Delta y = -1, 0, 1 \end{array} \right\} \quad (3)$$

where Δx and Δy are the increments of image coordinates in the X and Y directions, respectively.

Fig. 3 (A1) shows the detection of the seed points through the ZMIP process. In this figure, (A2) is the corresponding partially enlarged result of (A1). The figures show that the proposed method for seed-point detection can detect seed points within blood vessels and that the majority of vascular branches will be covered.

If some blood vessels overlap in one MIP direction in the projected image, then their vascular information will decrease, and the number of detected seed point will also decrease. Thus, we detect

new seed point sets $Seeds_x$ and $Seeds_y$ in XMIP and YMIP (Fig. 3(B1) and (C1)) to overcome this disadvantage and to obtain additional seed points. All seed point sets $Seeds_x$, $Seeds_y$, and $Seeds_z$ are merged to form the final set of seed points $Seeds_{xyz}$:

$$Seeds_{xyz} = Seeds_x \cup Seeds_y \cup Seeds_z \quad (4)$$

2.3. Vascular multiple-feature fusion image construction

After extracting seed points for vascular segmentation, a vascular multiple-feature fusion image is constructed on the basis of fuzzy inference, and three-dimensional vascular structures are segmented on the constructed fusion image. The vascular multiple-feature fusion image is generated by TOF and its corresponding vesselness image is obtained through multi-scale enhancement. Therefore, construction of the vascular multiple-feature fusion image can be divided into three steps: 1) multi-scale vascular enhancement, 2) fuzzy set transformation, and 3) vascular multiple-feature fusion.

2.3.1. Vesselness image

In this study, the corresponding vesselness image of TOF is obtained using the multi-scale vascular enhancement filter proposed by Frangi et al. (1998). The filter is constructed to detect the blood vessel region in accordance with the eigenvalue distribution of the Hessian matrix of tubular structures. The Hessian matrix $H(x, y, z)$ of pixel (x, y, z) can be expressed as follows:

$$H(x, y, z) = \begin{pmatrix} H_{xx} & H_{xy} & H_{xz} \\ H_{yx} & H_{yy} & H_{yz} \\ H_{zx} & H_{zy} & H_{zz} \end{pmatrix} \quad (5)$$

where H_{ij} ($i, j = x, y, z$) denotes partial derivatives in the i and j directions. Suppose that $H(x, y, z)$ is second-order continuous and $H(x, y, z)$ is a symmetrical square matrix. The three eigenvectors v_1 , v_2 and v_3 correspond to the directions of the vascular center-line and its cross section, and they are orthogonal to each other. The corresponding three eigenvalues λ_1 , λ_2 and λ_3 satisfy the following:

$$|\lambda_1| \approx 0 \quad (6)$$

$$|\lambda_1| \ll |\lambda_2| \quad (7)$$

$$\lambda_2 \ll \lambda_3 \quad (8)$$

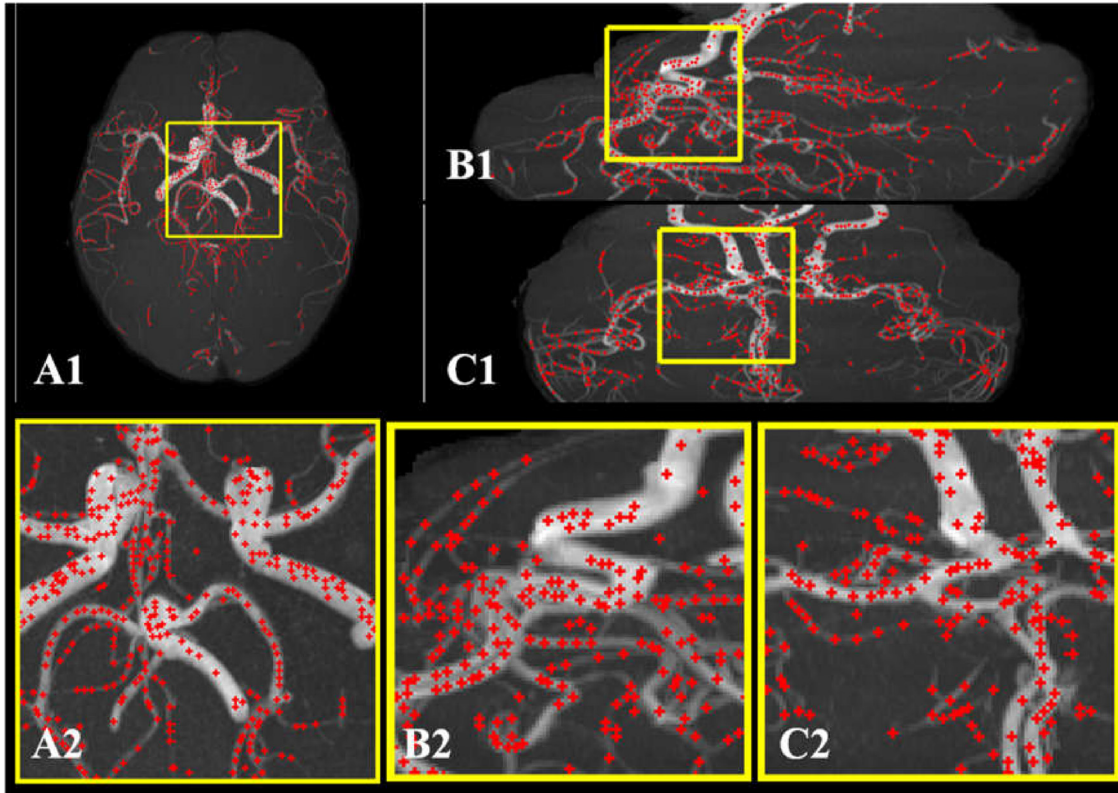


Fig. 3. Detected seed points in TOF image. (A1) Detected seed points in ZMIP. (A2) Enlarged of (A1). (B1) Detected seed points in XMIP. (B2) Enlarged of (B1). (C1) Detected seed points in YMIP. (C2) Enlarged of (C1).

According to this principle, the **vascular enhancement filter** can be constructed as follows:

$$v(x, y, z; \sigma) = \begin{cases} 0, & \text{if } \lambda_2 \text{ or } \lambda_3 > 0 \\ \left[1 - \exp\left(-\frac{R_A^2}{2\sigma^2}\right) \right] \exp\left(-\frac{R_B^2}{2\beta^2}\right) \left[1 - \exp\left(-\frac{R_C^2}{2\gamma^2}\right) \right], & \text{otherwise} \end{cases} \quad (9)$$

where, $R_A = \left| \frac{\lambda_2}{\lambda_3} \right|$, $R_B = \left| \frac{\lambda_1}{\lambda_2} \right|$, $R_C = \sqrt{\lambda_1^2 + \lambda_2^2 + \lambda_3^2}$, and σ corresponds to the Gaussian scale in Hessian matrix generation.

The TOF image contains blood vessels of various scales. Thus, the filter should be optimized in multi-scale space to enhance blood vessels of different scales. The **optimal vascular enhancement** can be obtained as follows:

$$v(x, y, z) = \max_{\sigma_{\min} \leq \sigma \leq \sigma_{\max}} v(x, y, z; \sigma) \quad (10)$$

where $[\sigma_{\min}, \sigma_{\max}]$ is the corresponding multi-scale space.

Fig. 4 (A1) shows a slice of TOF data and (A2) is its corresponding enlarged result. Fig. 4 (B1) shows the enhancement result of (A1) obtained using a multi-scale vascular enhancement filter, and (B2) shows its corresponding enlarged result. The figures show that using the multi-scale vascular enhancement filter significantly suppresses the background of non-vascular regions but enhances blood vessels. However, compared with those in the original TOF image, the **boundaries of blood vessels are drastically blurred** after vascular enhancement, leading to inconformity between the region of blood vessels and their real structures.

2.3.2. Fuzzy set transform

Images should be fuzzily processed, i.e., subjected to fuzzy set transformation, to fuse the vascular multiple feature of TOF and its corresponding vesselness image. In Fig. 5, let

the normalized intensity of the input image be T , and then the corresponding $N+1$ fuzzy sets $\{A_i\}_{i=1}^{N+1}$ can be expressed as $\{A_i\}_{i=1}^{N+1} = \{[T_0, T_1], [0, T_2], [T_1, T_3], \dots, [T_{N-1}, T_N], [T_N, T_{N+1}]\}$ ($T_0 = 0, T_{N+1} = 1$), and the fuzzy response of the A_i is denoted as $F_i(T)$. If the input T is in the area of $[T_N, 1]$, then the fuzzy response $F_N(T)$ is equal to 1. T_N can be considered as a segmentation threshold; when the T of the voxel v is larger than T_N , the confidence that v belongs to blood vessel is 1, i.e., v is completely a vascular voxel. When the input T is in the area of $[T_i, T_{i+1}]$, then T is only located in the area A_{i-1} of $[T_{i-1}, T_{i+1}]$ and A_i of $[T_i, T_{i+1}]$. $F_{i-1}(T)$ and $F_i(T)$ are not 0, whereas the rest are all equal to 0, i.e., $\{F_i(T)\} = \{0, \dots, F_{i-1}(T), F_i(T), \dots, 0\}$, where the response $F_{i-1}(T)$ and $F_i(T)$ can be expressed as follows:

$$F_{i-1}(T) = 1 - \frac{T - T_i}{T_j - T_i} \quad (11)$$

$$F_i(T) = \frac{T - T_j}{T_j - T_i} \quad (12)$$

2.3.3. Vascular multiple-feature fusion

In this study, a multi-premise, single-rule, fuzzy inference fusion framework is constructed on the basis of the fuzzy sets of TOF and its vesselness image. Let A be the fuzzy set of TOF image, B the fuzzy set of its vesselness, and C the fuzzy set of the output multiple-feature fusion. The fuzzy inference framework is constructed as follows:

Premise 1 (Truth): x is A' , and y is B' .

Premise 2 (Rule): If x is A and y is B , then z is C .

Conclusion: z is Z' .

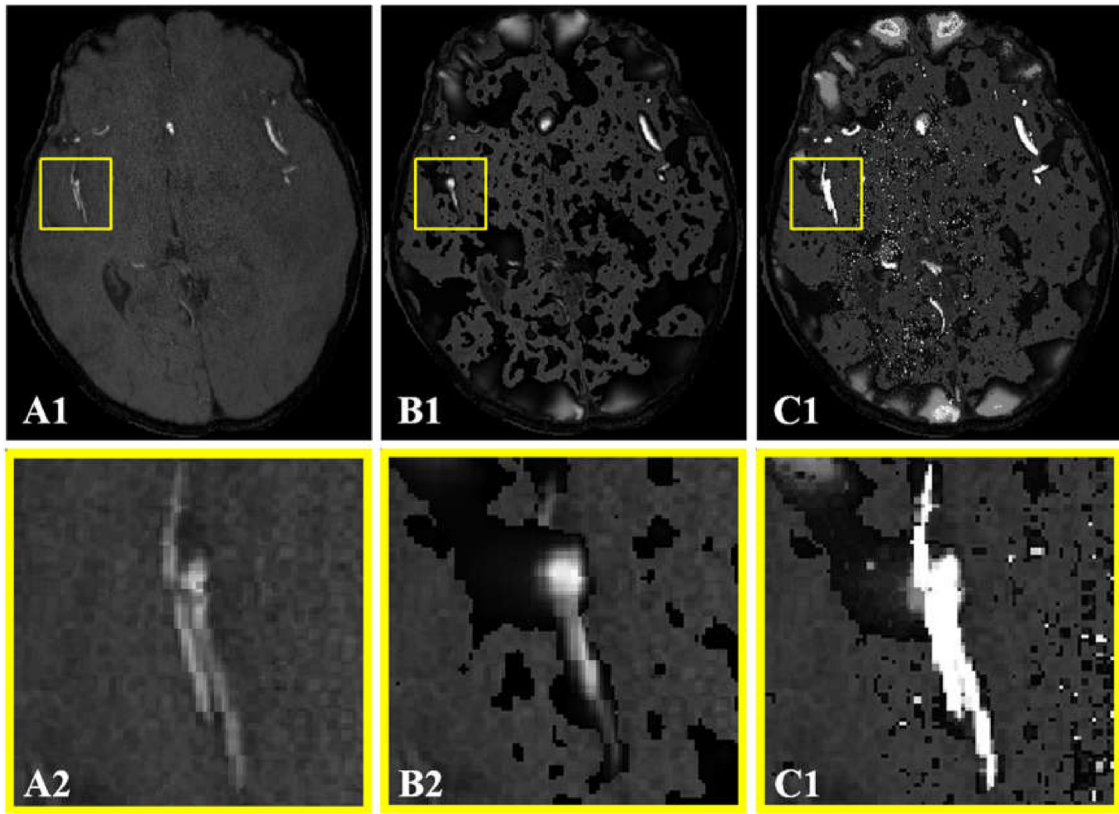


Fig. 4. (A1) Slice of TOF image. (A2) Enlarged of (A1). (B1) Multi-scale vascular enhancement result of (A1). (B2) Enlarged of (B1). (C1) Fuzzy inference-based vascular multiple-feature fusion result of (A1). (C2) Enlarged of (C1).

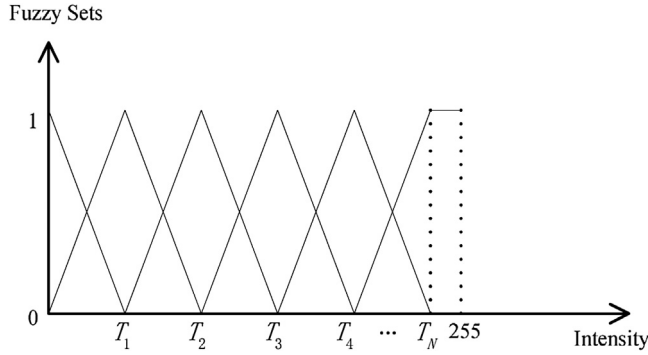


Fig. 5. Schematic of image fuzzy set transformation.

According to the Mamdani composition rule (Mamdani and Assilian, 1975), the obtained fuzzy membership $\mu_{C'}(z)$ can be expressed as follows:

$$\begin{aligned}
 \mu_{C'}(z) &= \bigvee_{x,y} [\mu_{A'}(x) \wedge \mu_{B'}(y)] \wedge [\mu_A(x) \wedge \mu_B(y) \wedge \mu_C(z)] \\
 &= \bigvee_{x,y} [\mu_{A'}(x) \wedge \mu_{B'}(y) \wedge \mu_A(x) \wedge \mu_B(y)] \wedge \mu_C(z) \\
 &= \left\{ \bigvee_x [\mu_{A'}(x) \wedge \mu_A(x)] \right\} \wedge \left\{ \bigvee_y [\mu_{B'}(y) \wedge \mu_B(y)] \right\} \wedge \mu_C(z) \\
 &= (\mu_A(x_0) \wedge \mu_B(y_0)) \wedge \mu_C(z)
 \end{aligned} \tag{13}$$

where “ \wedge ” and “ \vee ” are the minimum and maximum operators, respectively.

In Eq. (13), the multiple-feature fusion result depends not on the input fuzzy membership $\mu_A(x_0)$ and $\mu_B(y_0)$ but also on our defined fusion rules. A number of samples are trained to obtain suitable multiple-feature fusion rules for the fuzzy sets of TOF and its vesselness images.

After obtaining the output fusion fuzzy set C that corresponds to the TOF and its vesselness image, the multiple-feature fusion result z^* is calculated as the gravity center of fuzzy sets:

$$z^* = \frac{\int_z \mu_C(z) z dz}{\int_z \mu_C(z) dz} = \frac{\sum_{i=0}^N \mu_C(z_i) z_i}{\sum_{i=0}^N \mu_C(z_i)} \tag{14}$$

Fig. 4 (C1) presents a vascular multiple-feature fusion result based on the proposed fuzzy interference when N is equal to 5, and (C2) is the enlarged result of (C1). The figures show that multiple-feature fusion enhanced vascular structures relative to those in the original TOF image. However, some background regions are highlighted in addition to the blood vessels, therefore contributing some noisy areas. Extraction of blood vessel structures without noise thus becomes an important problem. Given that the seed points detected by the proposed method are all located in the true region of blood vessels and region growing proceeds in accordance with these seed points, the segmented blood vessels will be as close as possible to their real vascular structures.

3. Experimental result and discussion

Data from 12 clinical cases were randomly selected and tested in this study to evaluate the feasibility and effectiveness of the proposed algorithm. The clinical dataset comprises seven men and five women aged 14 to 50 years old (average age=30.6 years). The dataset was provided by Tsinghua University Imaging Center. The TOF datasets were evaluated on a 3T Philips Medical MRI Systems (Achieva) using a 32-

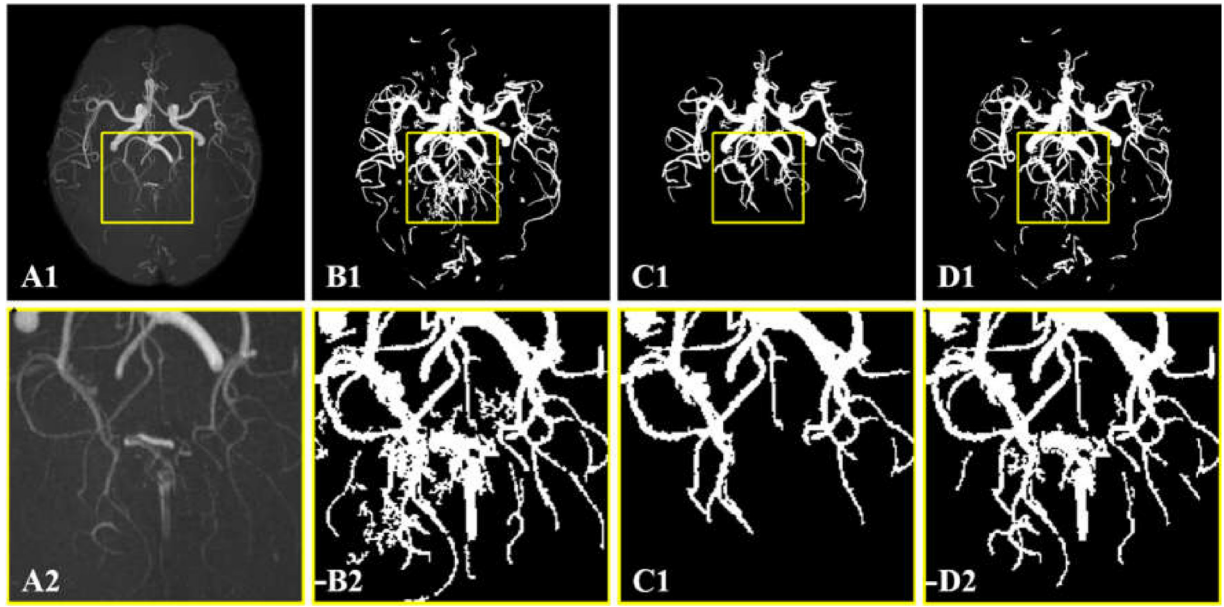


Fig. 6. MIP of the TOF and segmented three-dimensional vascular structures. (A1), (B1), (C1), and (D1) correspond to the MIP of the TOF brain volume segmented by the Chapman, Forkert, and proposed methods, respectively. (A2), (B2), (C2), and (D2) correspond to the enlarged images of (A1), (B1), (C1), and (D1), respectively.

channel head coil. The main angiography parameters were as follows: repetition time = 25 ms, echo time = 3.454 ms, flip angle = 15°, SENSE = 6, velocity-encoding value = 20 cm/s, resolution of obtained PC-MRA dataset = 528 × 528 × 150, and voxel size = 0.35 mm × 0.35 mm × 0.60 mm.

Chapman (Chapman et al., 2004) and Forkert algorithms (Forkert et al., 2011) are two typical cerebrovascular segmentation algorithms selected for comparison with the proposed method. In the Chapman algorithm, cerebrovascular structures are segmented through automatic seed-point detection and region growing in their corresponding original TOF image. In the Forkert algorithm, cerebrovascular structures are segmented on the basis of vascular multiple-feature fusion image and traditional region growing. In this study, the thresholding and multiple-feature fusion parameters of the algorithms were set at the same values to ensure a fair comparison.

First, the feasibility of the proposed algorithm for visualizing a segmented vascular structure was evaluated. Fig. 6 (A1), (B1), (C1), and (D1) correspond to the MIP of the TOF brain volume and were segmented by the Chapman, Forkert, and proposed methods, respectively. For the clear presentation of results, similar local regions in the images were enlarged and are shown in (A2), (B2), (C2), and (D2). Comparing (A2) and (B2) reveals that the Chapman algorithm resulted in excessive over-segmentation. Comparing (A2) and (C2) reveals that Forkert segmentation resulted in excessive under-segmentation. Comparing (A2) and (D2) reveals the proposed method provided segmentation results that are very similar to the actual vessel structures.

Fig. 7 shows the comparative segmentation results of the other two methods. (A1), (B1), and (C1) show the results of adding segmentation onto original slices when applying the Chapman, Forkert, and the proposed algorithms, respectively. (A2), (B2), and (C2) present the visualization results through marching cubes (Rajon and Bolch, 2003) with the application of the Chapman, Forkert, and proposed algorithms, respectively. Fig. 7 is very similar to Fig. 6. Segmentation using the Chapman algorithm resulted in over-segmentation. Applying the Forkert algorithm to segment cerebrovascular structures resulted in under-segmentation. When the proposed algorithm was applied, the segmented result was very close to its real structure. Therefore, the proposed algorithm can

provide highly accurate segmentation compared with other algorithms.

The manual segmentation of TOF by medical experts is the gold standard for the quantitative evaluation of segmentation results. Automatic segmentation by the Chapman, Forkert, and proposed algorithms were then compared. Dice similarity coefficient (DSC), false-positive rate (FPR), and false-negative rate (FNR) were used to quantify the segmentation, over-segmentation, and under-segmentation ratios, respectively, and were calculated in accordance with the literature (Wang et al., 2015) as follows:

$$DSC = \frac{2 \times (AS \cap GT)}{AS + GT} \quad (15)$$

$$FPR = \frac{AS \cap GT^c}{AS + GT} \quad (16)$$

$$FNR = \frac{AS^c \cap GT}{GT} \quad (17)$$

where AS and GT are the results of automatic and manual segmentations, respectively.

Table 1 shows the segmentation evaluation result of seed-point detection in the MIP of different directions for two datasets. X, Y, and Z correspond to the results of seed-point detection in XMIP, YMIP, and ZMIP, respectively. XY, XZ, and YZ correspond to the result of the union set of XMIP and YMIP, XMIP and ZMIP, and YMIP and ZMIP, respectively. As shown in the table, given that the projection resolution in the Z-axis direction of the data is 528 × 528 and that in the X- and Y-axis directions of the data is 150 × 528, the number of detected seed points in the Z-axis is larger than that in the X- and Y-axes. Therefore, DSC of ZMIP is larger than that of XMIP and YMIP. The addition of the detected seed point of XMIP and YMIP to the seed point set of ZMIP increases the number of detected seed points. Therefore, detection and merging method for seed points in the three axes of MIP can effectively ensure that the number of detected seed point increases as much as possible and that segmentation precision is as high as possible.

Table 2 shows the segmentation results of the Chapman, Forkert, and the proposed algorithms for 12 TOF datasets. The table shows that the average DSC corresponding to the proposed algorithm is 88.43%, which is 10.30% higher than that corresponding to the Chapman algorithm and 9.58% higher than that corresponding

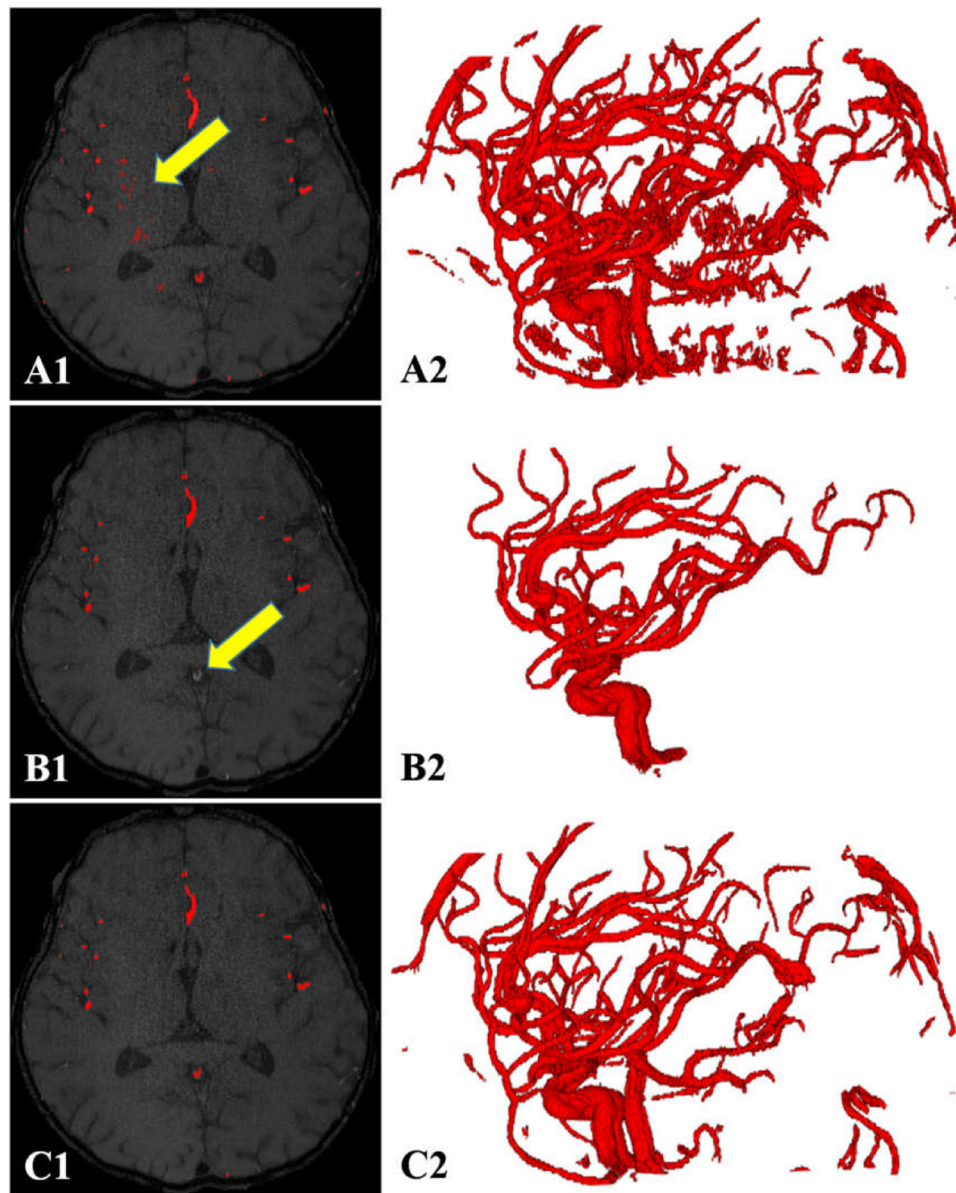


Fig. 7. Comparative segmentation result of different algorithms. (A1), (B1), and (C1) are the results of adding segmentation onto their original slices when Chapman, Forkert, and the proposed algorithms are applied, respectively. (A2), (B2), and (C2) are the visualization results by marching cubes when applying Chapman, Forkert, and proposed algorithms, respectively.

Table 1
Segmentation result of applying the proposed seed-point detection algorithm in the X, Y, Z, XY, XZ, YZ, and XYZ directions.

		X	Y	Z	XY	XZ	YZ	XYZ
Data1	NUM	1980	1742	4174	2649	5358	5181	
	DSC	93.42%	93.01%	93.64%	93.42%	93.64%	93.64%	
	FPR	3.65%	3.64%	3.86%	3.65%	3.86%	3.86%	
	FNR	9.15%	9.15%	8.56%	9.15%	8.56%	8.56%	
Data2	NUM	2013	2016	4971	2618	6058	6051	
	DSC	94.95%	94.90%	95.47%	94.95%	95.47%	95.47%	
	FPR	4.93%	4.82%	5.21%	4.93%	5.21%	5.21%	
	FNR	5.16%	5.35%	3.91%	5.16%	3.91%	3.91%	

to the Forkert algorithm. These values indicate that the segmentation structures of the proposed algorithm are closest to the manually segmented golden standard. In addition, the range of the DSC that corresponds to the proposed algorithm is [79.46%, 95.47%], which is smaller than the range of [62.92%, 91.24%] of the Chapman algorithm and [69.13%, 88.33%] of the Forkert algo-

rithm. These results indicate that the proposed algorithm is more stable than other algorithms. The average of FPR corresponding to the Chapman algorithm is 50.67%, which is higher than the 11.03% that corresponds to the Forkert algorithm and 17.69% that corresponds to the proposed algorithm. By contrast, the average of FNR corresponding to the Chapman algorithm is 1.04%, which is far lower than the 7.15% that corresponds to the Forkert algorithm and the 24.56% that corresponds to the proposed algorithm. These results indicate that when applying the three algorithms to segment cerebrovascular structures, the Chapman algorithm is prone to over-segmentation and the Forkert algorithm is prone to under-segmentation, as consistent with our previous conclusion. Applying the proposed algorithm to segment cerebrovascular structures ensures that not only the accuracy of segmentation is highest in the three algorithms, but also that over- and under-segmentation occur within a reasonable range. Therefore, the proposed cerebrovascular segmentation algorithm is superior to the Chapman and Forkert algorithms.

Table 2
Comparison of the segmentation results of the Chapman, Forkert, and proposed algorithms for 12 TOF datasets.

	Chapman algorithm			Forkert algorithm			Proposed algorithm		
	DSC	FPR	FNR	DSC	FPR	FNR	DSC	FPR	FNR
Data1	66.99%	94.69%	1.95%	88.33%	3.45%	18.17%	93.64%	3.86%	8.56%
Data2	76.90%	58.05%	1.25%	79.13%	25.97%	17.53%	79.46%	49.37%	1.53%
Data3	79.53%	50.72%	0.49%	82.94%	19.07%	15.63%	87.87%	25.83%	1.39%
Data4	62.92%	115.85%	0.92%	86.90%	5.77%	18.73%	94.22%	8.77%	3.11%
Data5	83.56%	38.57%	0.55%	81.63%	22.32%	15.64%	85.76%	32.06%	0.86%
Data6	91.24%	18.53%	0.57%	78.27%	1.53%	34.72%	83.10%	1.83%	27.62%
Data7	88.46%	24.44%	1.32%	87.31%	8.72%	15.75%	93.39%	11.15%	2.63%
Data8	77.58%	56.75%	0.65%	82.74%	2.55%	27.64%	93.43%	3.34%	9.39%
Data9	89.32%	23.46%	0.36%	69.13%	1.13%	46.58%	86.11%	1.77%	23.05%
Data10	81.71%	42.94%	1.26%	79.05%	2.31%	33.14%	95.47%	5.20%	3.91%
Data11	79.80%	48.23%	1.59%	79.65%	20.75%	20.08%	85.13%	32.13%	2.08%
Data12	84.06%	35.81%	1.52%	73.36%	18.85%	31.15%	83.58%	36.97%	1.67%
Mean	80.17%	50.67%	1.04%	80.70%	11.03%	24.56%	88.43%	17.69%	7.15%

4. Conclusions

The accurate segmentation of cerebrovascular structures from TOF-MRA datasets is important for diagnosis of cerebrovascular diseases and planning and navigation of neurosurgery. A novel cerebrovascular segmentation method is proposed in this study. The proposed method can be divided into four steps: brain mask detection, seed-point detection, vascular multiple-feature fusion, and region growing segmentation. In seed-point detection, seed points are extracted on the basis of MIP. Numerous seed points are located in blood vessels. Through this proposed automatic seed point detection method, vascular segmentation can be achieved without any human interaction, which is very time consuming. It can not only be used in region growing method, but also be served for any other seed point based vascular segmentation methods. To enhance the intensity information of vascular structures in the TOF-MRA image, the TOF image and its corresponding vesselness image are used to construct its vascular multiple-feature image based on fuzzy interference theory. The main advantage of the method is that it combines vascular multiple features and enhances the intensity information of vascular structures in the TOF-MRA image. It is very important for detection of tiny blood vessels, which can hardly be extracted by traditional methods. The detected seed points and vascular multiple-feature image are utilized for region-growing segmentation, and cerebrovascular structures can be automatically extracted from TOF-MRA data.

Data from 12 clinical cases were randomly selected and tested for the qualitative and quantitative evaluation of the performance of the proposed algorithm. In the qualitative analysis, the segmentation results were visualized by MIP, marching cubes, and fusion with their original slice. The segmentation results of the proposed algorithm are closer to their real structures than those of traditional algorithms. The manual segmentation of TOF-MRA operated by medical experts was utilized as the gold standard in quantitative analysis. The experimental results showed that the segmentation accuracy of the proposed algorithm is higher than that of traditional methods. In addition, the over- and under-segmentation of the proposed method are within a reasonable range. Therefore, our proposed cerebrovascular segmentation has potential clinical applications.

Conflict of interest

The authors declared that they have no conflicts of interest to this work.

Acknowledgments

This work was supported by National Key R&D Program of China (2017YFA0205904, 2016YFC 0105803), National Natural Science Foundation of China (81471759, 61701022), and the Fundamental Research Funds for the Central Universities (FRF-TP-16-045A1).

References

Ashburner, J., 2007. A fast diffeomorphic image registration algorithm. *Neuroimage* 38 (1), 95–113.

Aylward, S.R., Bullitt, E., 2002. Initialization, noise, singularities, and scale in height ridge traversal for tubular object centerline extraction. *IEEE Trans. Med. Imaging* 21 (2), 61–75.

Aylward, S., Bullitt, E., Pizer, S., Eberly, D., 1996. Intensity ridge and widths for tubular object segmentation and description. *IEEE/SIAM Workshop Math. Methods Biomed. Image Anal.*, 131–138.

Chapman, B.E., Stapelton, J.O., Parker, D.L., 2004. Intracranial vessel segmentation from time-of-flight MRA using pre-processing of the MIP Z-buffer: accuracy of the ZBS algorithm. *Med. Image Anal.* 8 (2), 113–126.

Cong, W., Yang, J., Ai, D., Chen, Y., Liu, Y., Wang, Y., 2015. Quantitative analysis of deformable model based 3-D reconstruction of coronary artery from multiple angiograms. *IEEE Trans. Biomed. Eng.* 62 (8), 2079–2090.

Du, X., Ding, H., Zhou, W., Zhang, G., Wang, G., 2013. Cerebrovascular segmentation and planning of depth electrode insertion for epilepsy surgery. *Int. J. Comput. Assist. Radiol. Surg.* 8 (6), 905–916.

Eskildsen, S.F., Coupé, P., Fonov, V., Manjón, J.V., Leung, K.K., Guizard, N., et al., 2012. BEaST: brain extraction based on nonlocal segmentation technique. *NeuroImage* 59 (3), 2362–2373.

Fischl, B., 2012. FreeSurfer. *Neuroimage* 62 (2), 774–781.

Forkert, N., Schmidt-Richberg, A., Fiehler, J., Illies, T., Möller, D., Handels, H., et al., 2011. Fuzzy-based vascular structure enhancement in time-of-flight MRA images for improved segmentation. *Methods Inf. Med.* 50 (1), 74.

Frangi, A., Niessen, W., Vincken, K., Viergever, M., 1998. Multiscale vessel enhancement filtering. In: *Medical Image Computing and Computer-Assisted Intervention—MICCAI'98*, pp. 130–137.

Friman, O., Hindennach, M., Kühnel, C., Peitgen, H.O., 2010. Multiple hypothesis template tracking of small 3D vessel structures. *Med. Image Anal.* 14 (2), 160–171.

Fritzsche, A.C.K., Shen, H., Tsai, C., Turner, J., Tanenbaum, H., Stewart, C., Roysam, B., 2003. Automated model based segmentation, tracing and analysis of retinal vasculature from digital fundus images. In: *Suri, J.S., Laxminarayan, S. (Eds.), State-of-The-Art Angiography, Applications and Plaque Imaging Using MR, CT, Ultrasound and X-Rays*, pp. 225–298.

Hassouna, M.S., Farag, A.A., Hushek, S., Moriarty, T., 2006. Cerebrovascular segmentation from TOF using stochastic models. *Med. Image Anal.* 10 (1), 2–18.

Kirbas, C., Quek, F., 2004. A review of vessel extraction techniques and algorithms. *ACM Comput. Surv.* 36 (2), 81–121.

Lesage, D., Angelini, E.D., Bloch, I., Funka-Lea, G., 2009. A review of 3D vessel lumen segmentation techniques: models, features and extraction schemes. *Med. Image Anal.* 13 (6), 819–845.

Mamdani, E.H., Assilian, S., 1975. An experiment in linguistic synthesis with a fuzzy logic controller. *Int. J. Man. Stud.* 7 (1), 1–13.

Masutani, Y., Schiemann, T., Höhne, K.-H., 1998. Vascular shape segmentation and structure extraction using a shape-based region-growing model. In: *Medical Image Computing and Computer-Assisted Intervention—MICCAI'98*. Springer, pp. 1242–1249.

Rajon, D., Bolch, W., 2003. Marching cube algorithm: review and trilinear interpolation adaptation for image-based dosimetric models. *Comput. Med. Imaging Graph.* 27 (5), 411–435.

Smith, S.M., Jenkinson, M., Woolrich, M.W., Beckmann, C.F., Behrens, T.E., Johansen-Berg, H., et al., 2004. Advances in functional and structural MR image analysis and implementation as FSL. *Neuroimage* 23 (S1), S208–S219.

Wang, R., Li, C., Wang, J., Wei, X., Li, Y., Zhu, Y., et al., 2015. Threshold segmentation algorithm for automatic extraction of cerebral vessels from brain magnetic resonance angiography images. *J. Neurosci. Methods* 241 (15), 30–36.

Wen, L., Wang, X., Wu, Z., Zhou, M., Jin, J.S., 2014. A novel statistical cerebrovascular segmentation algorithm with particle swarm optimization. *Neurocomputing* 148 (19), 569–577.

Xiao, R., Yang, J., Ai, D., Fan, J., Liu, Y., Wang, G., et al., 2015. Adaptive ridge point refinement for seeds detection in X-Ray coronary angiogram. *Comput. Math. Methods Med.* 2015.

Yang, J., Wang, Y., Liu, Y., Tang, S., Chen, W., 2009. Novel approach for 3-D reconstruction of coronary arteries from two uncalibrated angiographic images. *IEEE Trans. Image Process.* 18 (7), 1563–1572.

Yang, J., Cong, W., Chen, Y., Fan, J., Liu, Y., Wang, Y., 2014. External force back-projective composition and globally deformable optimization for 3-D coronary artery reconstruction. *Phys. Med. Biol.* 59 (4), 975–1003.